Wavefield-based AVO Inversion: Elastic images from pressure waves

Ettore Biondi, Biondo Biondi, and Robert Clapp

ABSTRACT

We introduce the concept of a wavefield-based amplitude variation with offset (AVO) inversion scheme. With this approach we do not make use high-frequency ray approximation or planar-reflector assumption used in most of the AVO inversion algorithms. We illustrate a method to compute elastic images by simple acoustic propagation of pressure waves, and demonstrate the equivalence with those obtained by full elastic wavefield modeling.

INTRODUCTION

AVO inversion is a fundamental step in seismic exploration to quantitatively characterize subsurface elastic properties (Foster et al., 2010). From the inverted physical parameters, reservoir analysis and simulations can be conducted (Simm et al., 2014). Since the first discussion on AVO by Ostrander (1982), many techniques have been proposed to perform AVO inversion (Hampson, 1991; Castagna, 1993). In recent years, Bayesian non-linear and linearized AVO inversion applications have been published (Buland and Omre, 2003; Rabben et al., 2008), thanks to the speedup of computational resources.

Despite the capability of extensively exploring big model spaces in the context of AVO characterization and inversion, most existing AVO schemes are affected by the assumptions behind the full or linearized Zoeppritz equations (Aki and Richards, 2002). The first assumption is that a plane wave is impinging on an interface across which elastic properties vary; and hence, that the incident wavefield can be decomposed into a superposition of plane waves. Secondly, the interface separating two media has to be locally planar where the plane wave interacts with it. Considering plane waves during AVO inversion inherently assumes the ray approximation. However, the ray approximation does not correctly account for the Fresnel zone of the band-limited signals employed during a seismic experiment. The planar interface assumption is critical, especially when dealing with complex subsurface geological structures (Etgen et al., 2009), where the assumption breaks down. Therefore, given our interest in characterization of deep and subsalt reservoirs it is necessary to develop an AVO inversion approach that is not based on these assumptions.

We start by illustrating the mathematical background of the wavefield-based AVO inversion scheme. We then describe the first step necessary to conduct such an AVO

inversion, computing elastic images (i.e., the full waveform inversion (FWI) gradient) using acoustically propagated wavefields. We proceed with this operation because we are only interested in inverting the PP reflected energy. On a single reflector model we demonstrate the equivalence of these images to those generated by a full elastic FWI scheme. In our synthetic test the new approach is five times computationally cheaper compared to the corresponding full elastic method.

WAVEFIELD-BASED AVO INVERSION

As shown by Innanen (2014) there exists a neat equivalence between linearized AVO inversion and precritical reflection FWI based on Gauss-Newton Hessian inversion. Innanen's discussion is developed for non-constant density acoustic media; although we do not show this connection for elastic reflectors, we expect it to hold for elastic media as well. In addition, when the correct background model is used to perform FWI we should obtain the correct reflectivity by a single Gauss-Newton step (Biondi et al., 2015). Therefore, with a single Gauss-Newton inversion step for an elastic FWI problem we expect the same result we would obtain by performing linearized AVO inversion in the case of simple planar reflectors. However, in the former we are not considering the same assumptions as in the latter.

The goal of both FWI and AVO inversion is to predict the amplitudes of the recorded data with an elastic model. The primary difference is that FWI tries to invert for all the scales of the model; whereas, in AVO inversion we are interested in finding perturbations of the background model. We start with the usual FWI amplitude-matching objective function defined as follows:

$$\phi(\mathbf{m}) = \frac{1}{2}\left(\mathbf{d}_{\text{pre}} - \mathbf{d}_{\text{obs}}\right) = \frac{1}{2}\left(\mathbf{R}\mathbf{f}(\mathbf{m}) - \mathbf{d}_{\text{obs}}\right), \tag{1}$$

where $\mathbf{d}_{\text{obs}}$ represents the recorded data, and $\mathbf{d}_{\text{pre}}$ the predicted data, that is given by a combination of the wavefield extraction operator $\mathbf{R}$ and the non-linear elastic modeling operator $\mathbf{f}(\mathbf{m})$, in which $\mathbf{m}$ is the model vector that for the isotropic elastic case can be parametrized in terms of first Lamé's parameter λ, shear modulus μ, and density ρ. The recorded data can be pressure or multicomponent data. As previously mentioned, we are interested in performing a single Gauss-Newton step of this non-linear problem. Therefore, our goal is to solve the following linear system:

$$\mathbf{H}_{GN}(\mathbf{m}_0)\mathbf{\Delta m} = -\nabla\phi(\mathbf{m}_0), \tag{2}$$

where $\mathbf{H}_{GN}(\mathbf{m}_0)$ and $\nabla\phi(\mathbf{m}_0)$ represent the Gauss-Newton Hessian matrix and gradient of the objective function in equation 1, both evaluated at the background model $\mathbf{m}_0$; $\mathbf{\Delta m}$ is the elastic reflectivity that we wish to retrieve and should match the one we would obtain by applying an AVO inversion algorithm. Despite the higher computational cost of wavefield-based AVO inversion, we expect this new method to correctly account for the Fresnel zone of influence of the transmitted signals when dealing with complex subsurface geometry. Therefore, it will go beyond the approximations made in common AVO inversion methods.

ELASTIC IMAGES FROM PRESSURE WAVES

In this section we show that we can compute an elastic FWI gradient using only acoustically propagated P-waves when a smooth background is considered as starting model. Therefore, we can save computational time because we do not have to proceed with any full elastic propagation. Assuming that we are interested in only inverting PP energy recorded at our receivers, we are able to compute the gradient of the objective function defined in equation 1 using acoustically propagated wavefields. In fact, if our initial model does not contain sharp property contrasts we can neglect the mode conversions and separate the propagation of P-wave and S-wave modes from each other (Zhang and Weglein, 2009). When the spatial derivatives of the background model are small (i.e., when the background model is smooth enough), this approximation is valid because the nonlinear propagation operator can be diagonalized.

For our discussion, we use the velocity-stress formulation of the isotropic elastic wave equation (Virieux, 1986). In this formulation the effect of recording data using only hydrophones is that the data are given by the arithmetic average of the propagated normal stress at the receiver positions. Alves (2015) shows how to implement the adjoint Born operator in the velocity-stress formulation in order to compute the gradient of equation 1. The imaging condition for each parameter of the λ, μ, and ρ parametrization can be written as follows:

$$\begin{aligned}
\nabla_\lambda \phi &= -\int_0^t \left(\frac{\partial v_{x,s}}{\partial x} + \frac{\partial v_{z,s}}{\partial z} \right) (\sigma_{xx,r} + \sigma_{zz,r}) \; dt, \\
\nabla_\mu \phi &= -\int_0^t 2\frac{\partial v_{x,s}}{\partial x}\sigma_{xx,r} + 2\frac{\partial v_{z,s}}{\partial z}\sigma_{zz,r} + \left(\frac{\partial v_{x,s}}{\partial z} + \frac{\partial v_{z,s}}{\partial x} \right) \sigma_{xz,r} \; dt, \\
\nabla_\rho \phi &= \int_0^t \dot{v}_{x,s} v_{x,r} + \dot{v}_{z,s} v_{z,r} \; dt,
\end{aligned} \tag{3}$$

where v_x and v_z are the wavefields of the particle velocities, σ_{xx} and σ_{zz} the normal stress wavefields, and σ_{xz} the shear stress wavefield. In these equations the subscripts s and r correspond to the source wavefields and the adjoint receiver wavefields, respectively. Each kernel in equation 3 effectively represents an image of a given model parameter. For brevity we have omitted the spatial and time dependence of the wavefields. The first two kernels can be rewritten in terms of elastic strain components, yielding the following equations:

$$\begin{aligned}
\nabla_\lambda \phi = & -\int_0^t \left(\dot{\varepsilon}_{xx,s} + \dot{\varepsilon}_{zz,s} \right) \left(\varepsilon_{xx,r} + \varepsilon_{zz,r} \right) \left(\lambda_0 + 2\mu_0 \right) \; dt, \\
\nabla_\mu \phi = & -2\int_0^t \lambda_0 \left(\dot{\varepsilon}_{xx,s} + \dot{\varepsilon}_{zz,s} \right) \left(\varepsilon_{xx,r} + \varepsilon_{zz,r} \right) \\
& +2\mu_0 \left(\dot{\varepsilon}_{xx,s}\varepsilon_{xx,r} + \dot{\varepsilon}_{zz,s}\varepsilon_{zz,r} + \dot{\varepsilon}_{xz,s}\varepsilon_{xz,r} \right) \; dt,
\end{aligned} \tag{4}$$

where λ_0 and μ_0 are the elastic parameters of the background model. It is interesting that these two kernels have a term in common up to a scaling factor. However, the shear modulus has a contribution from the shear strains that is not present in the λ kernel that can separate the two parameters.

As discussed at the beginning of this section, the propagation of P-wave and S-wave modes can be separated in a slowly varying background model. Because we are interested in matching the PP event amplitudes we can compute the necessary source and receiver wavefields by propagating pressure fields. In fact, by knowing any pressure wavefield $p(x,z,t)$ we can easily compute the particle displacements $\mathbf{u}(x,z,t)$ from:

$$\mathbf{u}(x,z,t) = \frac{1}{\rho(x,z)} \int_{\tau=0}^{t} \left(\int_{0}^{\tau} \nabla p(x,z,\tau') d\tau' \right) d\tau, \tag{5}$$

that represents the particle movements caused by a pressure exerted on a volume element (Aki and Richards, 2002). From the particle displacements we can compute the strain components generated by the propagating pressure wave as follows:

$$\begin{aligned} \varepsilon_{xx}(x,z,t) &= \tfrac{\partial u_x(x,z,t)}{\partial x}, \\ \varepsilon_{zz}(x,z,t) &= \tfrac{\partial u_z(x,z,t)}{\partial z}, \\ \varepsilon_{xz}(x,z,t) = \tfrac{1}{2}\left(\tfrac{\partial u_x(x,z,t)}{\partial z} + \tfrac{\partial u_z(x,z,t)}{\partial x} \right) &= \tfrac{\partial u_x(x,z,t)}{\partial z} = \tfrac{\partial u_z(x,z,t)}{\partial x}, \end{aligned} \tag{6}$$

where the equalities in the shear strain follow from equation 5 and Schwartz' theorem. From the particle velocities and strain components of the source and receiver wavefields we are able to compute the imaging conditions of equations 4. Now, the only problem with equation 5 is that the receiver wavefield is computed backward in time (Fichtner, 2010; Almomin, 2013; Biondi and O'Reilly, 2015). It is necessary to perform the backward propagation and store the total adjoint wavefield in memory to compute the particle displacements. This issue could limit the applicability of the proposed method, but it can be resolved with a simple assumption. If we consider that at the final propagation time t_f the particles are at rest, we can write:

$$\begin{aligned} \mathbf{u}(x,z,t_f) = 0 = \frac{1}{\rho(x,z)} \int_{\tau=0}^{t_f} \left(\int_{0}^{\tau} \nabla p(x,z,\tau') d\tau' \right) d\tau \Rightarrow \\ \int_{\tau=t_f}^{t} \left(\int_{t_f}^{\tau} \nabla p(x,z,\tau') d\tau' \right) d\tau = \int_{\tau=0}^{t} \left(\int_{0}^{\tau} \nabla p(x,z,\tau') d\tau' \right) d\tau, \end{aligned} \tag{7}$$

so we can integrate backward in time for the particle displacements. Therefore, we can avoid storing the total adjoint wavefield in memory.

Equivalence of the elastic gradients: synthetic test

In this section we compare the elastic images obtained by cross-correlating acoustically propagated wavefields with the gradient computed using the full elastic operators developed by Alves (2015). Figure 1 shows the model used to perform this synthetic test where the background velocities are $V_p = 2500\,\mathrm{m/s}$, $V_s = 1000\,\mathrm{m/s}$ and a single interface is placed at 900 m. In the test we used 230 sources and 485 receivers evenly spaced by 14 m and 7 m, respectively. Figure 2 displays a single

shot gather in which the recorded reflection presents a phase variation as the source-receiver distance increases. By applying an elastic Born operator on this data we obtain the elastic images shown in Figure 3(b). In Figure 3(a) we display the elastic gradient computed by cross-correlating wavefields that have been propagated with an acoustic propagator (Biondi and O'Reilly, 2015). The two elastic gradients are equivalent besides negligible differences (i.e., five orders of magnitude smaller than the energy of the images). The λ image differs from the μ image because we have employed enough offset information so that the extra term in equation 4 is effectively contributing. From a computational perspective the images on Figure 3(a) are five times less computationally intensive compared to the images generated by full-elastic wavefields.

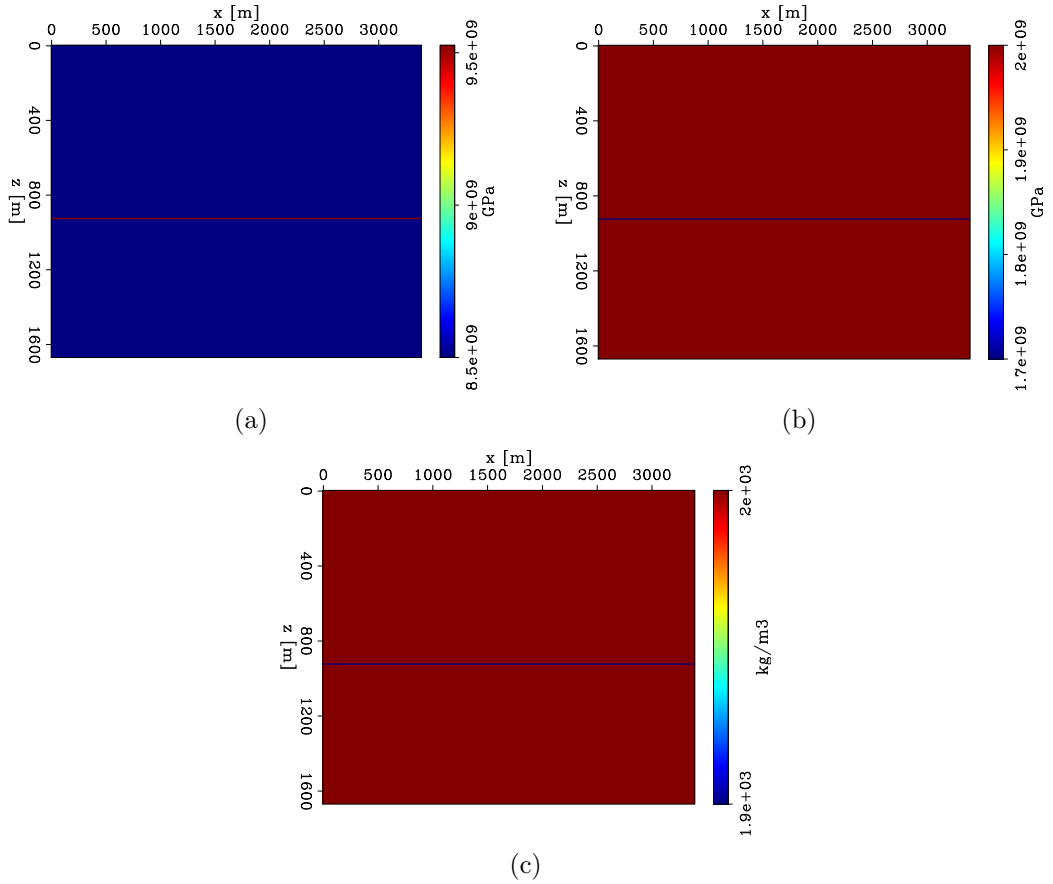

Figure 1: (a) First Lamé's parameter, (b) shear modulus, and (c) density models with a single interface. This model's properties correspond to a background velocities and density of $V_p = 2500\,\mathrm{m/s}$, $V_s = 1000\,\mathrm{m/s}$, and $\rho = 2000\,\mathrm{kg/m^3}$. [**ER**]

CONCLUSIONS AND FUTURE RESEARCH DIRECTION

We have presented a new AVO inversion scheme based on wavefield propagations. This new method does not require all the approximations that common AVO inversion

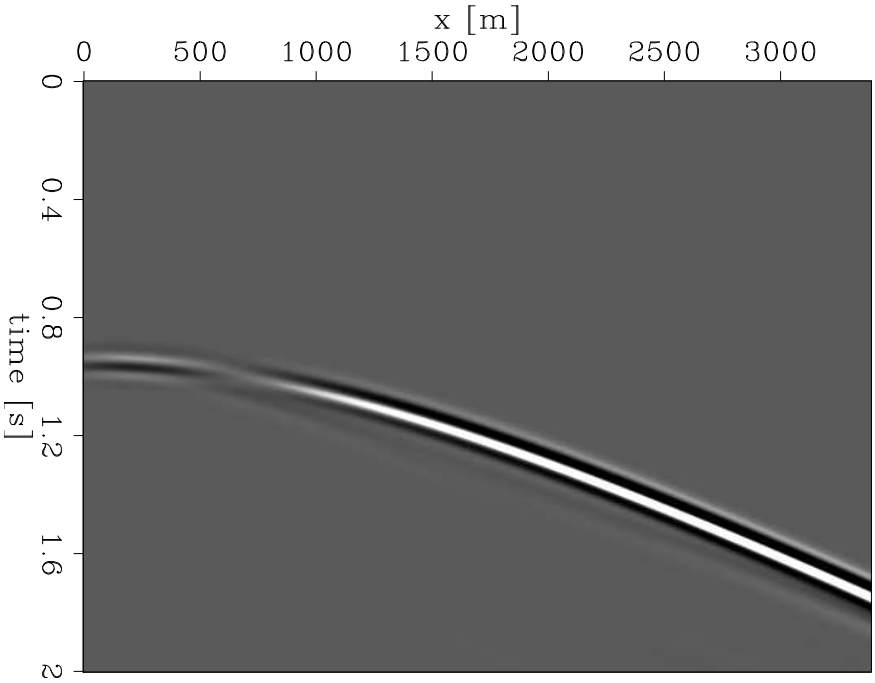

Figure 2: Reflection data for a single shot generated by the elastic interface shown in Figure 1. In this reflection, we have phase variations with offset that cause the wavelet to have opposite polarity for small reflection angles compared to higher offsets. [**CR**]

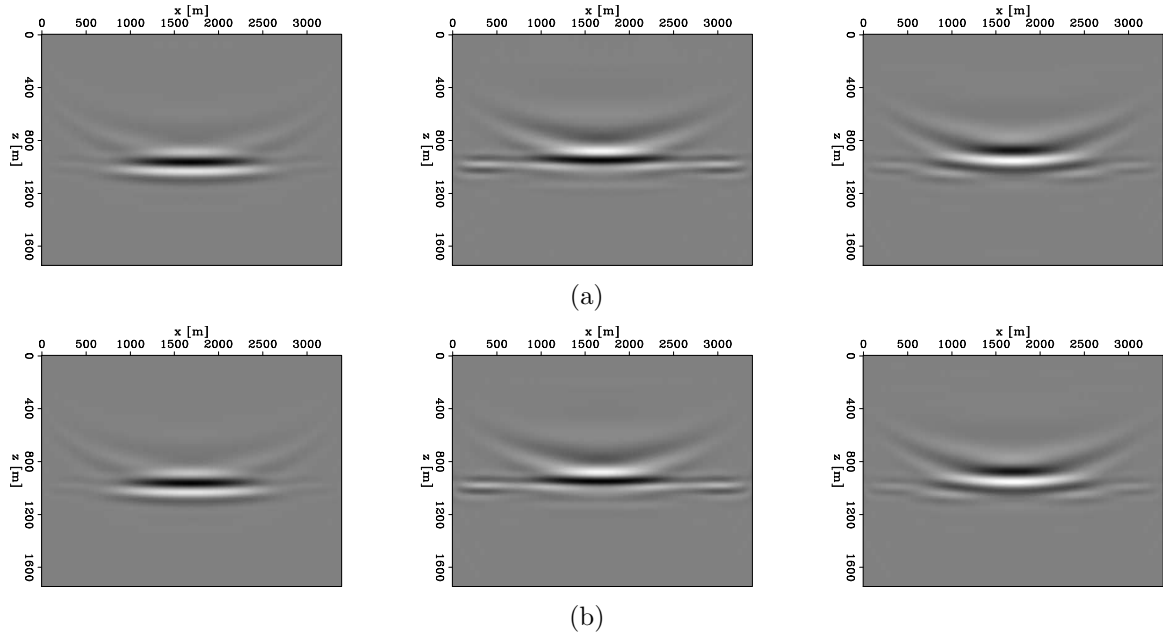

Figure 3: Comparison between elastic images generated by acoustically propagated wavefields and full elastic ones. (a) Elastic images from acoustic pressure waves. (b) Elastic images from full elastic pressure waves. On the left column images for λ, in the center images for μ, and on the right column images for ρ. Besides small difference not detectable from the figure the gradients are equivalent. [**CR**]

techniques usually include, such as ray approximation and flat reflection interfaces. In this paper, we have shown how to perform the first step of this process: elastic FWI gradient computation. For the purpose of inverting PP events only, we are able to compute an elastic FWI gradient from acoustically propagated pressure fields. We have compared full elastic images to ones computed by the proposed algorithm, and shown their equivalence on a one-reflector model. In future reports, we will explore the connection between FWI and AVO inversion. In particular, we want to understand the relation between the linearized AVO equation and the Born approximation commonly used in FWI. We will also compare inversion results from the AVO inversion and the proposed method on simple layered models in which the two methods should provide the same inversion results, as well as on complex subsurface models in which we expect the approximations of common AVO inversion to be a limiting factor during the inversion. In addition to this comparison, we will also explore the added value of using a Gauss-Newton Hessian as opposed to a full Hessian matrix. We believe that the second-order scattering information given by the full Hessian matrix can help us to resolve complex interface geometries.

REFERENCES

Aki, K. and P. G. Richards, 2002, Quantitative seismology, volume **1**.

Almomin, A., 2013, Accurate implementation of two-way wave-equation operators: SEP-Report, **149**, 281–288.

Alves, G., 2015, Adjoint formulation for the elastic wave equation: SEP-Report, **158**, 133–150.

Biondi, B., E. Biondi, M. Maharramov, and Y. Ma, 2015, Dissection of the full-waveform inversion Hessian: SEP-Report, **160**, 81–100.

Biondi, E. and O. O'Reilly, 2015, Two-way wave-equation operators for non-constant density acoustic isotropic media: SEP-Report, **160**, 19–38.

Buland, A. and H. Omre, 2003, Bayesian linearized AVO inversion: Geophysics, **68**, 185–198.

Castagna, J. P., 1993, Offset-dependent reflectivity: theory and practice of AVO analysis: Society of Exploration Geophysicists.

Etgen, J., S. H. Gray, and Y. Zhang, 2009, An overview of depth imaging in exploration geophysics: Geophysics, **74**, WCA5–WCA17.

Fichtner, A., 2010, Full seismic waveform modelling and inversion: Springer Science & Business Media.

Foster, D. J., R. G. Keys, and F. D. Lane, 2010, Interpretation of AVO anomalies: Geophysics, **75**, 75A3–75A13.

Hampson, D., 1991, Avo inversion, theory and practice: The Leading Edge, **10**, 39–42.

Innanen, K., 2014, Reconciling seismic AVO and precritical reflection FWI-analysis of the inverse Hessian: SEG Technical Program Expanded Abstracts 2014, 1022–1027, Society of Exploration Geophysicists.

Ostrander, W., 1982, Plane wave reflection coefficients for gas sands at nonnormal angles of incidence: Presented at the 1982 SEG Annual Meeting.

Rabben, T. E., H. Tjelmeland, and B. Ursin, 2008, Non-linear Bayesian joint inversion of seismic reflection coefficients: Geophysical journal international, **173**, 265–280.

Simm, R., M. Bacon, and M. Bacon, 2014, Seismic Amplitude: An interpreter's handbook: Cambridge University Press.

Virieux, J., 1986, P-SV wave propagation in heterogeneous media: Velocity-stress finite-difference method: Geophysics, **51**, 889–901.

Zhang, H. and A. B. Weglein, 2009, Direct nonlinear inversion of multiparameter 1d elastic media using the inverse scattering series: Geophysics, **74**, WCD15–WCD27.